Topographic Modification of the Florida Current by Little Bahama and Great Bahama Banks

KEVIN D. LEAMAN

Rosenstiel School of Marine and Atmospheric Science, University of Miami, Miami, FL 33149

ROBERT L. MOLINARI

National Oceanic and Atmospheric Administration, Atlantic Oceanographic and Meteorological Laboratory, Miami, FL 33149

ABSTRACT

The effect of local topography in modifying the structure and variability of the Florida Current is examined using shipboard acoustic Doppler and PEGASUS acoustic current profiler data. PEGASUS absolute velocity data were obtained during 16 cruises in the Florida Current at 27°N as part of the Subtropical Atlantic Climate Studies (STACS) program. The ensemble average of all PEGASUS velocity data shows that the effect of the constriction imposed on the mean Florida Current by Little Bahama Bank can be detected up to 30 km into the Straits of Florida. A simple model is proposed to explain how this effect can produce the subsurface maximum of northward flow commonly observed in the eastern Straits.

PEGASUS and acoustic Doppler data obtained during the March 1984 STACS cruise are used to describe the temporal and spatial variability of the flow. It is shown that intermittent southward flow can exist in a band 10–15 km wide off Little Bahama Bank; one such event was detected during this cruise. The PEGASUS data suggest that these events are associated with meandering of the Florida Current. These results may explain earlier observations in satellite synthetic aperture radar images of small-scale vortices moving southward across the mouth of Northwest Providence Channel.

1. Introduction

Leaman et al. (1987) describe a series of recent observations collected in the Straits of Florida as part of the Subtropical Atlantic Climate Studies (STACS) Florida Current experiment. A more complete description of this experiment is given in a series of recent papers (Molinari, 1983; Larsen and Sanford, 1985; Lee et al., 1985; Marmolejo, 1985; Maul et al., 1985; Molinari et al., 1985; Schott and Zantopp, 1985). Temperature and velocity data were obtained using the acoustic ocean current profiler, PEGASUS (Spain et al., 1981). The STACS results confirm earlier findings which show that variability observed in the velocity structure of the Florida Current on day-to-week time scales is comparable to variability observed on the seasonal time scale. A variety of causes (e.g., continental shelf waves) has been suggested to explain this variability. We here consider the possibility that some of the variability is produced by interaction of the Florida Current with the local topography of Great Bahama Bank (GBB) and Little Bahama Bank (LBB), Fig. 1. Few previous current studies have been made in this region and even the mean flows away from the Straits are unknown (Richardson and Finlen, 1967; Lee, 1977; Hine et al., 1981, for instance).

In order to examine the structure of the eastern boundary of the Florida Current in greater detail, the NOAA Ship *Researcher* made a set of Acoustic Doppler Current Profiler (ADCP) observations from LBB to Bimini during a March 1984 cruise (Fig. 1). These data and PEGASUS data collected along the STACS section are used to study the mean and time-dependent flow of the eastern Straits. In the next section we will describe the methods used to process the PEGASUS and ADCP data. Following this, the distinctive features of the eastern boundary flow as seen in the two datasets will be presented. Finally, one possible mechanism which may account for the observed features will be discussed.

2. Analysis of PEGASUS and ADCP datasets

PEGASUS is a free-fall, acoustically tracked profiler of absolute horizontal ocean currents and temperatures. Details of its use in STACS and analyses of errors have been given elsewhere (Leaman et al., 1987; Leaman and Vertes, 1983) and will only be briefly summarized here. At each STACS PEGASUS station (Fig. 1) repeated velocity profiles were obtained from within about 5 m of the surface to about 5 m of the bottom during each of the 16 STACS PEGASUS cruises. The vertical resolution of each original profile was 3–4 m. To simplify further processing and analysis, profiles were interpolated and subsampled to 10 m depth increments. Estimated errors in the north velocity component are typically 0.01 m s^{-1} at all stations. The east velocity component errors can range up to 0.03 m s^{-1} in the high speed surface core of the Florida Current.
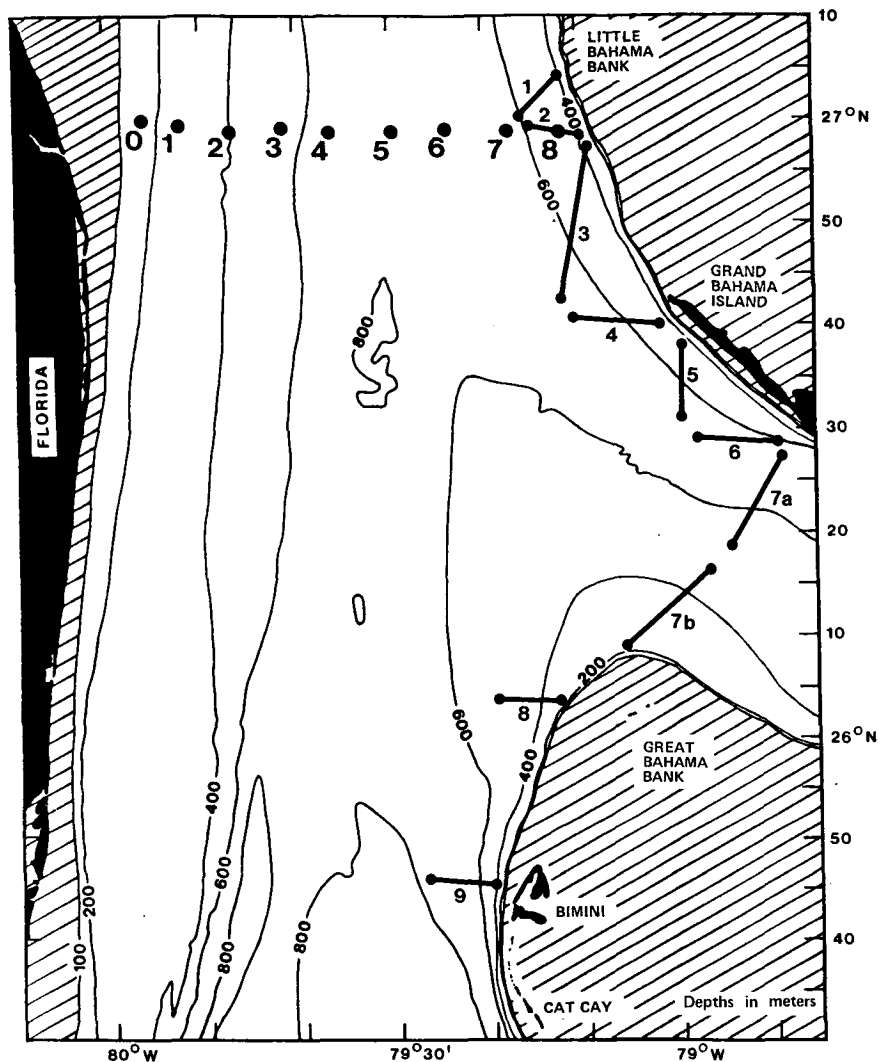
FIG. 1. Location of STACS PEGASUS stations (0–8) and ADCP sections (1–9) made by the NOAA vessel *Researcher* in March 1984. The ends of each ADCP section shown in Fig. 3 are indicated by the solid dots.

Toward the eastern boundary, east and north component errors are both typically 0.01 m s^{-1}.

Based on details of the Florida Current structure observed near the eastern boundary by PEGASUS, a survey of currents along LBB, GBB and Northwest Providence Channel (NWPC) was made using a shipboard ADCP from the NOAA Ship *Researcher* on 17–18 March 1984. Locations of the sections are shown in Fig. 1. Along each section, ADCP profiles were obtained at a rate of 35 raw profiles per minute. These profiles were then averaged to obtain one average ADCP relative profile per minute along the ship track. Ship-relative velocities were obtained in 63 depth bins, each of width 6.4 meters. The center of the first bin is located 10.2 m below the sea surface.

The ship's velocity must be known to derive absolute velocity profiles from relative ADCP profiles. (The

"bottom-track" mode of the ADCP was found to be unreliable and was not used.) LORAN-C provided the only continuous position coverage during the March 1984 cruise. Unfortunately, the accuracy of LORAN-C derived positions in the eastern Straits is poor, primarily because the lines of constant time delay for different station pairs intersect at relatively shallow angles. The orientation of these lines is such that any noise in time delays will introduce a large (up to 0.5 n mi) apparent excursion in position along a line directed roughly 340°T/160°T. Also, it was found that the LORAN-C receivers used in the experiment themselves introduce a quasi-periodic (period ~3 min) wandering along this line.

For purposes of later analysis, the velocities along each section were rotated into a right-handed coordinate system in which the u component is positive into

a boundary (such as LBB) and the v component is parallel to the boundary. The rotation angles used for each ADCP section shown in Fig. 1 are given in Table 1 (positive anticlockwise). Sections 8 and 9 were not rotated because the edge of GBB is strongly curved in this area. In what follows the u and v components will refer to these rotated coordinates for each section (PE-GASUS data along 27°N were not rotated).

To estimate ship velocity along each section, raw one-minute positions were first-differenced to provide an initial set of u and v ship velocity components. Points at the start and end of each section (where the ship was changing course) were excluded. A least-squares quadratic fit (including a sinusoid with 3-min period to remove the LORAN-C receiver induced wandering) was then passed through the u and v component estimates. Thirteen points were used to obtain reasonable estimates of ship velocity. Points beyond two standard deviations of the residual away from the fit were excluded and the fit was repeated. The resulting fitted ship velocity estimates at each of the 13 points were added to the corresponding ADCP relative profiles to obtain absolute profiles. The 13 absolute profile estimates were then averaged to provide a smoothed absolute velocity profile at the center of the window. For typical ship speeds of 10 kt this provided a spatial smoothing along each section with a typical scale of 3.6 km. In regions with better LORAN-C coverage this spatial resolution could be improved considerably. Table 1 shows the standard error ($\sigma/\sqrt{N}$) of the rotated ship velocity components for each section described below. (Because of a small but rapid course change, section 7 was split into two parts. An average coordinate rotation angle was used for sections 7a and 7b.) The relatively higher error levels for v compared to u reflect the anisotropy of LORAN-C position errors referred to above.

A similar standard error can be obtained for the residuals about the 13-point average ADCP relative velocities computed for each depth bin. As expected, the largest residual variances in the relative profiles are

TABLE 1. Standard errors of ship velocity components.

Section	Rotation angle (deg)	Standard error (m s⁻¹)	
		u	v
1	18	0.04	0.12
2	18	0.04	0.11
3	25	0.03	0.10
4	25	0.05	0.17
5	43	0.06	0.16
6	43	0.07	0.12
7a	50	0.08	0.15
7b	50	0.06	0.12
8	0	0.08	0.09
9	0	0.08	0.15

found at the maximum acoustic ranges from the ship (380–410 m) and indicate that an upper bound on the standard error of either relative velocity component is approximately 0.07 m s⁻¹. This shows clearly that in this region navigational errors are the major source of uncertainty in deriving absolute velocities.

3. Structure of the mean flow along the eastern boundary

The structure of the mean east and north velocity component and temperature fields as estimated from the ensemble average of all PEGASUS profiles made during the STACS cruises is shown in Fig. 2. Also shown are the standard deviations of these fields. These can be used to evaluate the stability of the means based on an estimated 40 independent observations (over all STACS cruises) for each mean value (Leaman et al., 1987).

The most obvious feature of the east velocity component is a region of negative (westward) flow which is strongest at LBB and extends some 30 km to the west into the Straits of Florida. At LBB a maximum in westward flow is observed at 180 m, with the largest vertical shear concentrated above the maximum. A subsurface maximum in the north velocity at LBB is observed over the same depth range as the maximum in westward flow (Fig. 2). As a result, the near-surface vertical current shear is reversed relative to the typical shear observed further west.

These results can be compared with the mean fields observed further south at the latitude of Miami by Ni-iler and Richardson (1973). In their data there is some indication of a subsurface maximum in the north velocity component in winter; however, it is not as intense as observed off LBB and it is not present in summer. The east velocity component further south remains positive in both seasons but, at least above 200 m, decreases toward GBB.

The mean horizontal velocity vectors near the eastern boundary exhibit a marked directional stability with depth away from the surface (or bottom). At station 8 between 110 m and 490 m the average current bearing is 346°T and no individual current vector deviates by more than ±3° from this average. Within 30 m of the bottom the mean current vectors veer slightly to the right with increasing depth. Of greater interest here, above 100 m the mean currents also veer to the right and flow almost due north within 50 m of the surface. The most rapid veering occurs at 100–110 m, at the top of the thermocline (25°C, Fig. 2c).

4. Current variability and flow reversals along Little Bahama Bank

Cross sections of the absolute along-boundary velocity component (v) observed by ADCP during the March 1984 cruise are shown in Fig. 3a–i. The component normal to the boundary (u) is not shown since
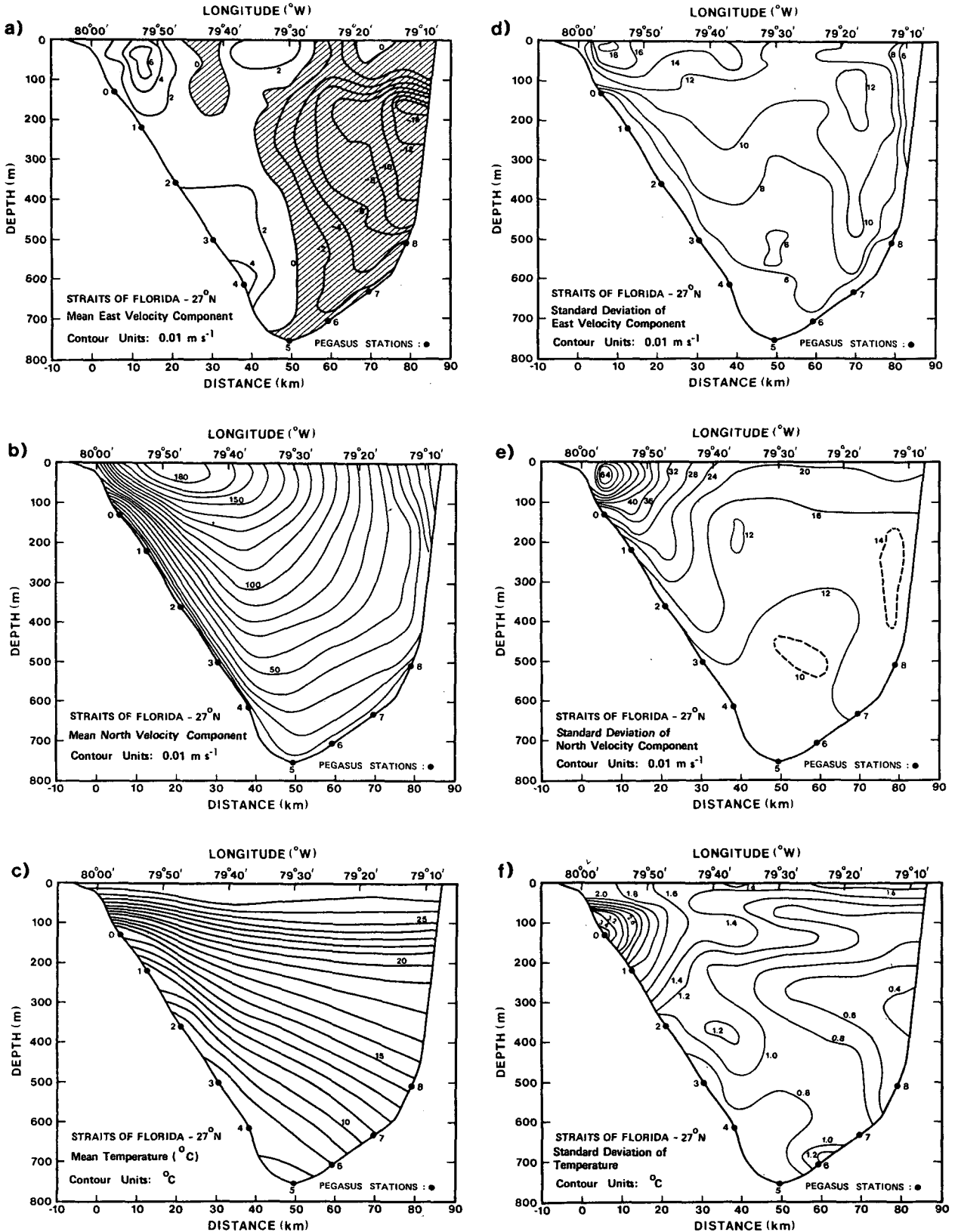
FIG. 2. The ensemble average (a–c) and standard deviation (d–f) of east and north velocity components and temperature, respectively, based on results of 16 STACS PEGASUS cruises to the Florida Current at 27°N.
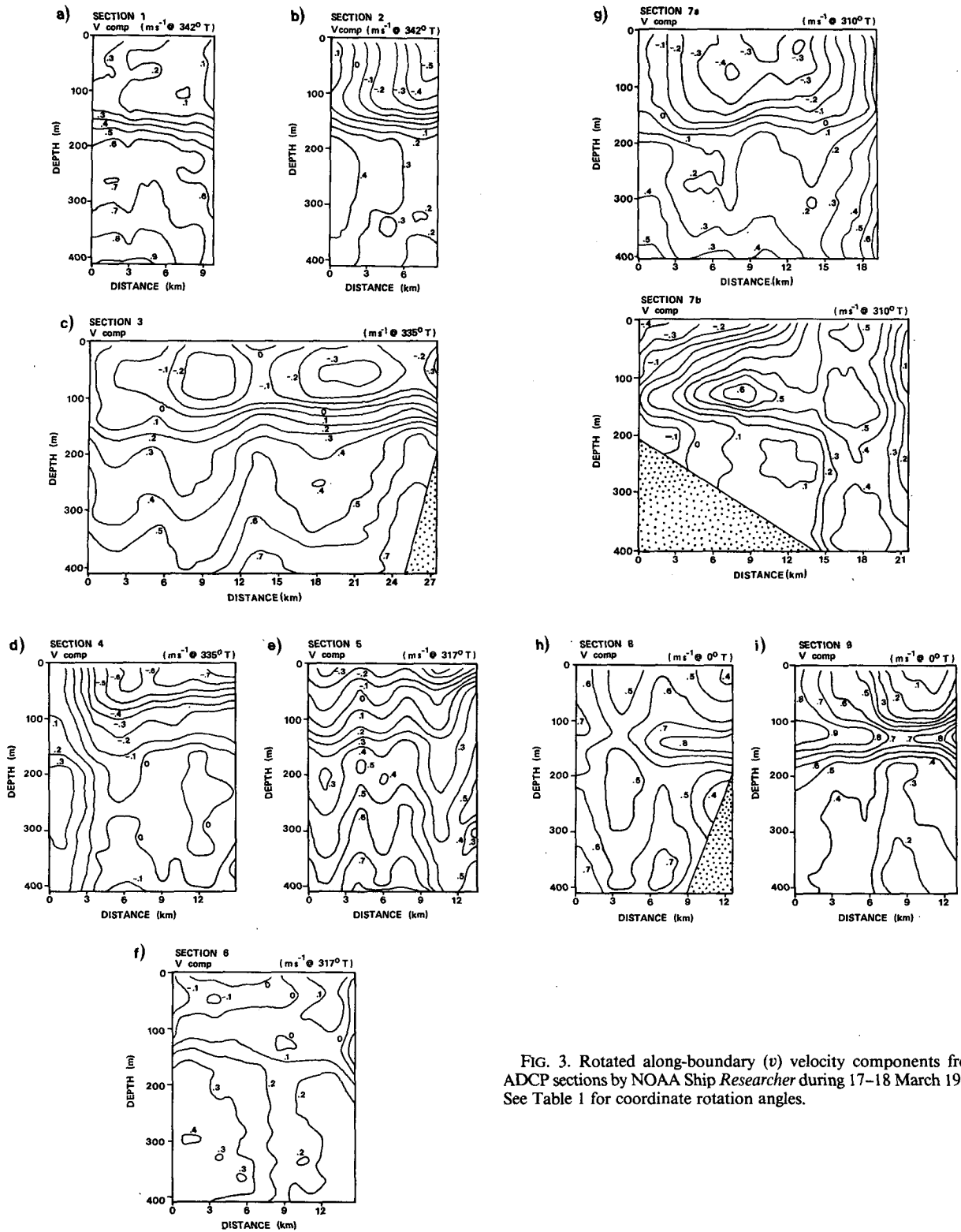
FIG. 3. Rotated along-boundary (v) velocity components from ADCP sections by NOAA Ship *Researcher* during 17–18 March 1984. See Table 1 for coordinate rotation angles.

with few exceptions it is not significantly different from zero (Table 1). The start and end of each section are shown in Fig. 1 by dots, and the distance origin for each section in Fig. 3 is the southern or western end. Some general features observed in the average PE-GASUS section are also present in the northernmost

ADCP sections 1–2. In particular, a large negative shear in the along-boundary component is concentrated at depths of 100–150 m. In general, a subsurface velocity maximum is not observed in the ADCP data; however, Fig. 2 suggests that on the average the along-boundary component begins to decrease again only at depths below 400 m. The most obvious difference between the average PEGASUS section and the northern ADCP sections is that in the latter the flow has actually reversed near the surface along LBB. We will describe in more detail the space and time evolution of this event shortly.

Sections 4, 5 and 6 end at the solid boundary of Grand Bahama Island. A region of reverse shear in the v component, which decays away from the boundary, can be traced at least through section 4. The termination of this region is not as evident in sections 5 and 6, although section 6 ends relatively farther away from the boundary than the other sections and is also nearly parallel to the boundary.

Sections 7 (a and b) provide a cross section of absolute currents across the western end of NWPC. This section is characterized by eastward flow in the northern half and westward flow in the southern half. At the southern end, near GBB, a region of high v-component shear at 100–150 m depth is also seen. However, in contrast to what is observed in the northern sections, flow here is concentrated in the form of a relatively narrow jet flowing into the Straits of Florida and reaching speeds of 0.6 m s^{-1}. [The absolute velocity contours of section 7b from 15 km to 20 km distance are somewhat doubtful. These contours indicate that a sudden "pulse" in ship speed occurred, although we have found no evidence of this in ship navigation data. Since ship positions were recorded once per minute while $\sim$35 ADCP profiles were averaged over the same interval, the effect of a short-period (<1 min) deviation in ship track could not be removed by the fitting procedure described above.]

Finally, sections 8 and 9 are once again in the Straits of Florida but to the south of NWPC. In both cases the flow along the boundary (approximately the v component) is characterized by a relatively thin jet between 100 and 150 m. This is similar to the subsurface maximum observed off LBB but is of smaller amplitude and is much more concentrated in depth. In section 8 this flow decays away from the boundary. Although section 8 velocity components have not been rotated, the contours of this "jet" (Fig. 3h) in v and u (not shown) indicate that it tends to follow the north-northeastward tilt of GBB at this location. In section 9 the same jet is present; however, it appears to be divided into two "peaks." The eastern peak again flows against GBB, while another peak is found about 12 km into the channel.

The unexpected observation of near-surface flow reversal along LBB led us to reexamine all STACS PEGASUS cruises to estimate the frequency of such events. (In what follows we take "near-surface" to be the observed flow at 20 m to avoid extrapolation of profiles which did not quite reach the surface.) Of the 16 cruises, flow reversals were observed in six (June, September and November 1982; September 1983; January and March 1984) at station 8. There is no clear correlation with season or magnitude of Florida current transport. Of these six cruises the March 1984 event was by far the strongest (southward surface flow $\sim$0.43 m s^{-1}); southward flow events during the remaining cruises were generally <0.1 m s^{-1} except June 1982 ($\sim$0.15 m s^{-1}). For this reason we will concentrate on a description of the March 1984 event.

Figures 4 and 5 show the temporal and spatial evolution of this event. In Fig. 4 contours of the east and north velocity components relative to the time mean at each depth are shown for station 8. The southward flow anomaly is of short duration ($\sim$1–2 days) and is confined mainly to the upper 150 m. In contrast to the average PEGASUS section (Fig. 2), during the period of southward flow there exists an eastward flow component.

To examine east–west variations with time, Fig. 5(a–f) shows the behavior of depth-averaged east and north velocity components along the PEGASUS section together with fluctuations of these components at 20 m (within the depth-range of the event) and 220 m (below the event), relative to the depth-averaged currents. Barotropic tides have been removed from the north velocity component, based on Mayer et al. (1984). For any station let $W(z_i, t_j)$ be the east (u) or north (v) velocity component observed at a depth z_i and profile time t_j, where observations are available at N_z depths (every 10 m) and N_T profiles. Then the quantities shown in Fig. 5 are defined as:

$$\bar{W}(t_j) = \frac{1}{N_z} \sum_{i=1}^{N_z} W(z_i, t_j) \tag{1a}$$

$$\langle \bar{W} \rangle = \frac{1}{N_T} \sum_{j=1}^{N_T} \bar{W}(t_j) \tag{1b}$$

$$\bar{W}' = \bar{W}(t_j) - \langle \bar{W} \rangle \tag{1c}$$

$$W'(z_0, t_j) = W(z_0, t_j) - \langle W(z_0) \rangle \tag{1d}$$

where

$$\langle W(z_0) \rangle = \frac{1}{N_T} \sum_{j=1}^{N_T} W(z_0, t_j) \tag{1e}$$

for $z_0 = 20$ or 220 m.

The depth and time averaged east (north) velocity components [Eq. (1b)] are shown in the upper panels of Fig. 5a and 5d, while the time-averaged east (north) velocity components at 20 and 220 m [Eq. (1e)] are given respectively in the upper panels of Fig. 5b and 5c (5e and 5f).
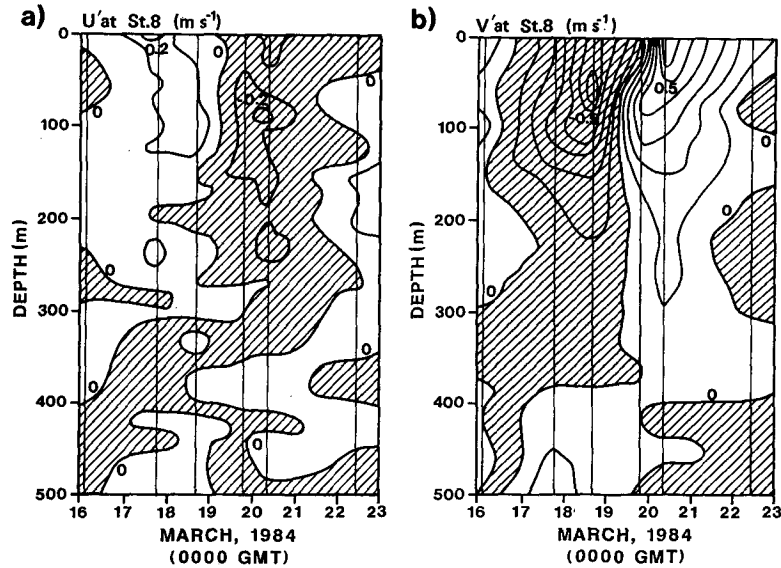
FIG. 4. Anomalies relative to the time mean at each depth of (a) east and (b) north velocity components observed at PEGASUS station 8 in March 1984.

The tendency of the depth-averaged north component (Fig. 5d) to show an east-west alternation of positive and negative anomalies is characteristic of meandering of the Florida current axis (Leaman et al., 1987). The period of southward flow along LBB is clearly associated with a negative anomaly which appears in the eastern half of the Straits in the middle of the cruise. A comparison of the north components at 20 and 220 m during this event shows that the shear between these levels (Fig. 5e minus Fig. 5f) decreases and in comparison to the anomaly in depth-averaged north velocity component is more strongly trapped against the eastern boundary. In agreement with Fig. 4 most of the shear variation takes place in the upper layer and the variations in the lower layer tend to be smaller and of the opposite sign. During the period of southward anomaly an eastward anomaly is observed at the eastern boundary, in agreement with Fig. 4.

5. Discussion

The concentration of negative vertical shear of the along-boundary velocity component at thermocline depths (24°-25°C) of 100-150 m near LBB is a common feature of the average PEGASUS dataset (Fig. 2) as well as of PEGASUS or ADCP data obtained during individual cruises. On the other hand, comparison of data from all PEGASUS cruises indicates that strong flow reversals along the boundary (e.g., >0.1 m s^{-1}) are relatively uncommon. The observations suggest two questions: 1) what establishes the average current field near LBB (Fig. 2) and 2) why the flow occasionally reverses.

A possible mechanism which may help to explain question 1 is suggested by the local LBB topography

near 27°N. Over most of its depth this boundary is almost a vertical wall which moreover is oriented at roughly 340°T.

As pointed out above, the average direction of currents observed below 110 m depth at PEGASUS station 8 is 346° ± 3°T. Since we expect that as the Florida Current flows north and hits LBB it is forced to flow parallel to the eastern boundary ($\sim$340°T) at these depths, the close agreement of the directions quoted above is not surprising. However, nearer the surface (above 50-100 m depth) the LBB is not a solid boundary. The data indicate that the mean flow remains northward (i.e., with a component onto LBB) in agreement with earlier results from sparse current meter data obtained over LBB in the same area (Hine et al., 1981). We hypothesize that through a geostrophic adjustment process the flow will be modified as it is constrained to change direction at the boundary. Furthermore, since the boundary allows fluid to be removed near the surface but not deeper (i.e., the lateral forcing is not depth-independent), part of the adjustment process will produce baroclinic modes that decay away from LBB. The type of topographic boundary described above can be modeled by a simple steady-state system (see the Appendix). The model boundary allows the mean northward flow of the Florida Current to continue above a certain depth but forces the flow to deviate to the west below the depth. The water is assumed to be stratified with a peak in the stability frequency at about 120 m depth, as observed.

The decay (e-folding) scales for the first three baroclinic modes in the model are found to be 20.86, 8.63 and 5.76 km, respectively, suggesting that at least the lowest 2-3 modes should be observable in the PE-
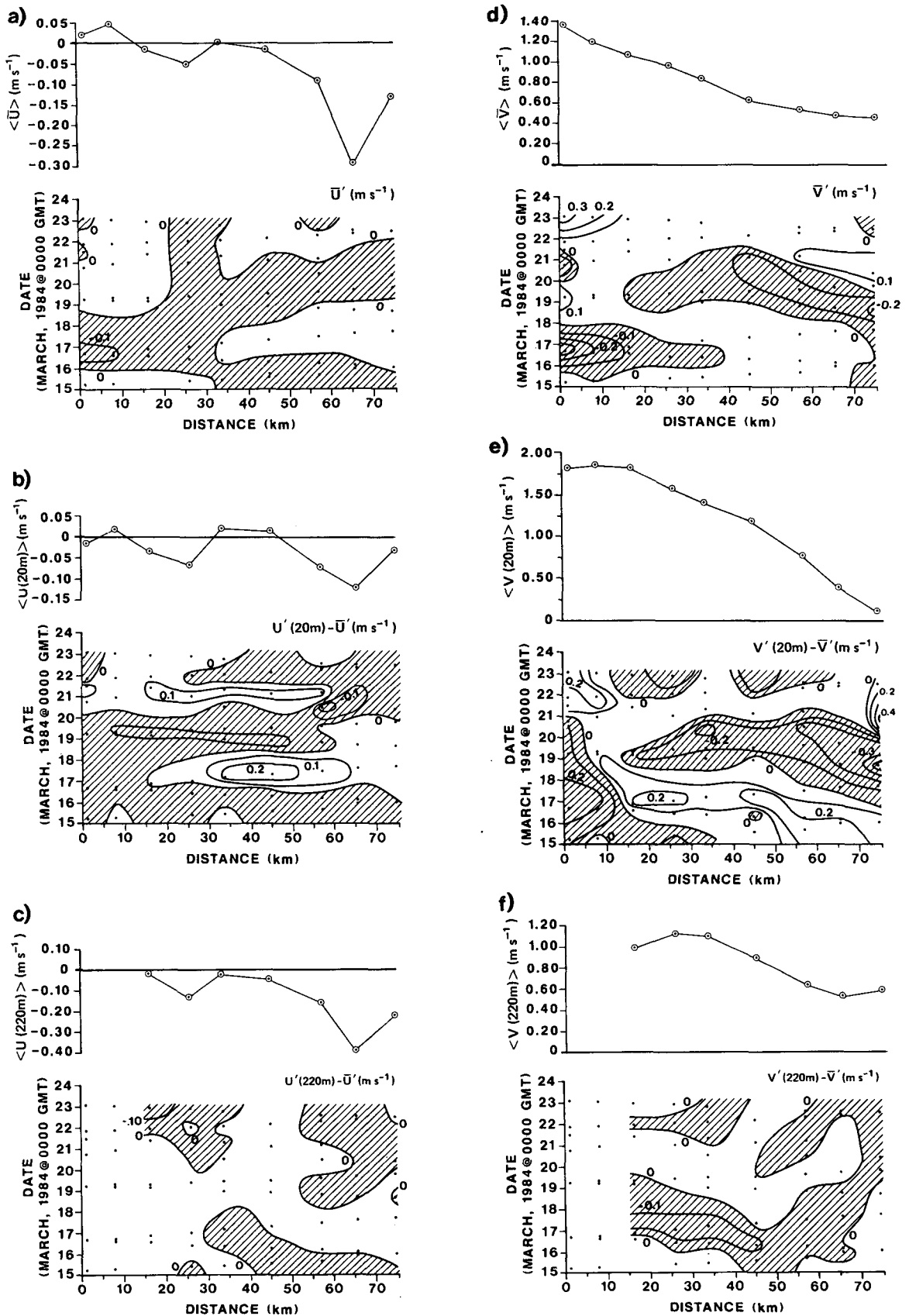
FIG. 5. Anomalies of (a–c) east and (d–f) north velocity components for the depth-averaged flow (a, d) and for the flow at 20 m (b, e) and 220 m (c, f) depths relative to the depth-averaged flow, in March 1984. Time averages across the Straits of Florida, from which these anomalies were computed, are shown in the upper panels. In these graphs, an overbar denotes a depth average, angle brackets ⟨ ⟩ denote a time average, and a prime denotes the anomaly from the time-averaged value.
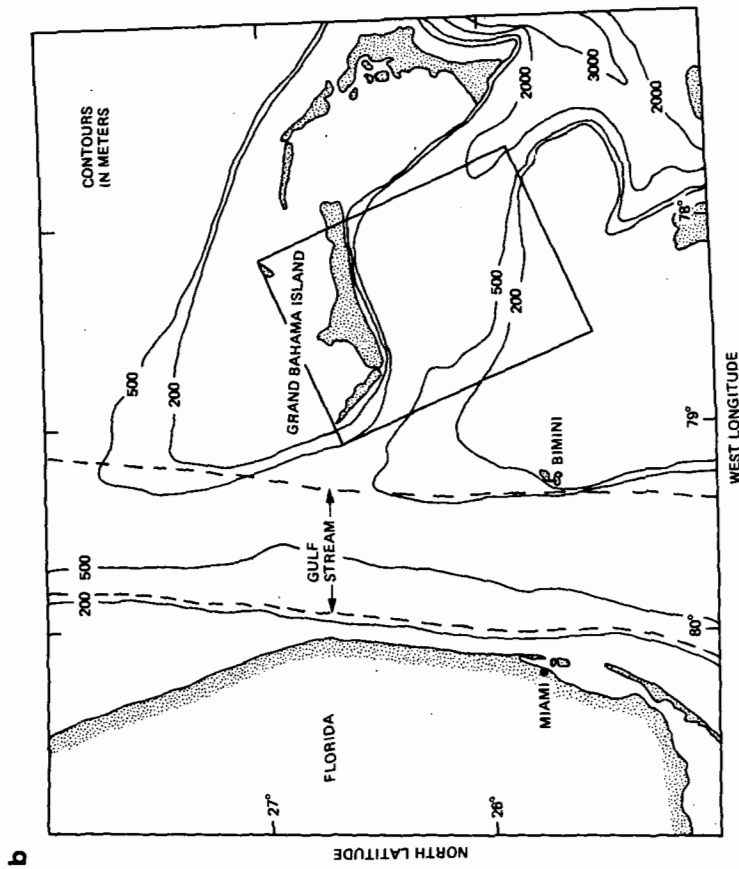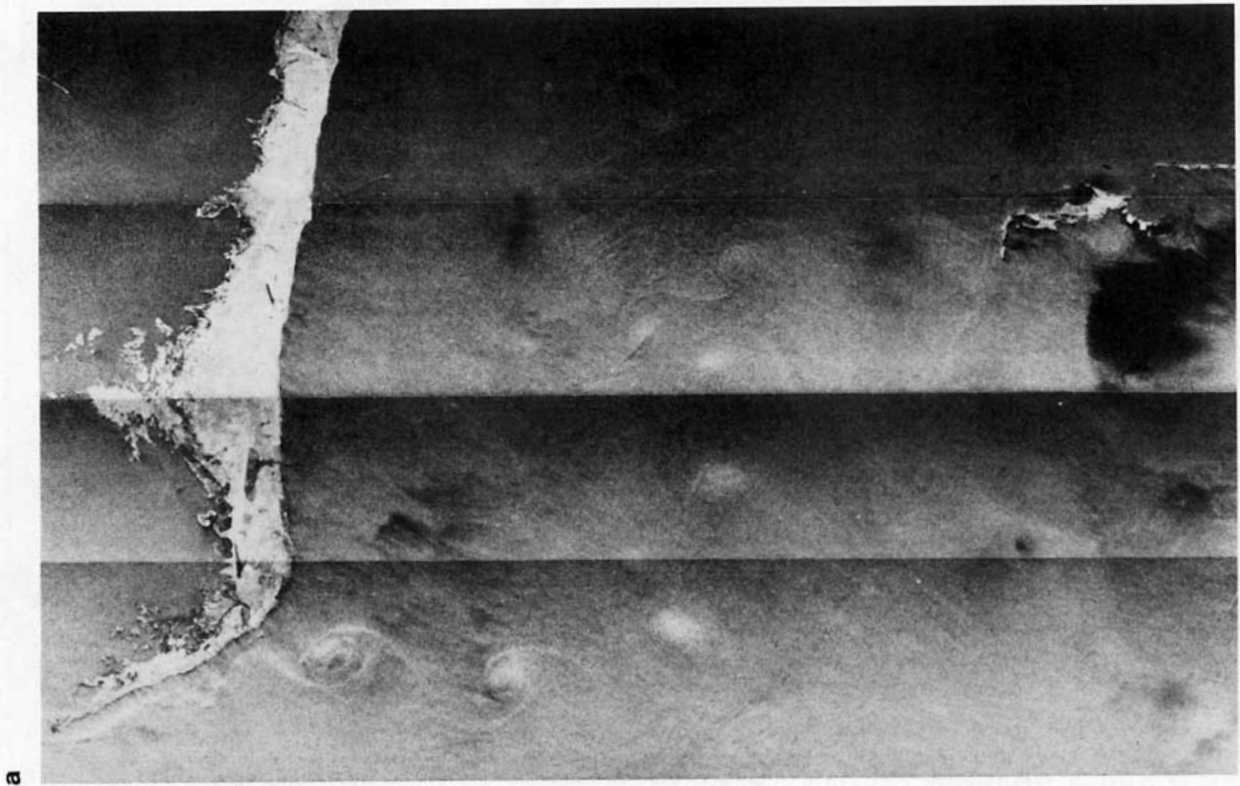
FIG. 6. (a) SAR image of Grand Bahama Island made at 1325 UTC on 27 September 1978, and (b) a chart showing the geographic orientation of this image. The southward extent of these eddies corresponds well with the northern edge of Grand Bahama Bank, after which additional eddies are found on a line to the east (after Fu and Holt, 1982).

GASUS data. In fact, the decay scale for the lowest mode is in reasonable agreement with the observed decay of the mean westward flow away from LBB. The peak in stability frequency at depths ∼120 m serves mainly to concentrate the vertical shear within this depth region, as observed. Finally, results of this simple model indicate that the along-boundary velocity component will exhibit negative vertical shear near the surface. Physically this arises because the boundary forces a small upward motion at middepths, thereby producing negative relative vorticity and thus a decrease of the along-boundary velocity component near the boundary.

A more complicated extension of the above model would be needed to quantify the temporal variability and the appearance of flow reversals described above. Figure 5 suggests that these events are related to larger scale variations in the Florida Current. The March 1984 data show that southward flow, when it occurs, is concentrated in the upper 100–150 m and is confined to a region within 10–15 km of LBB. During this time the depth-averaged north velocity component showed a negative anomaly broadly distributed over the eastern half of the Florida Current, consistent with what is commonly observed during periods of meandering. A negative anomaly could, by shifting the basic shear profile (Fig. 2), produce southward flow at the surface; however, Fig. 5 suggests that this is not the whole story. In particular, during this event the negative vertical shear observed at PEGASUS station 8 also intensified near the boundary. Although the mechanism that produces this is not clearly understood and the data are sparse, the temporal evolution of these reductions in northward flow observed during March 1984 is similar to the evolution during other cruises. In particular, if anomalies in the east and north velocity components relative to cruise mean values are computed at station 8 during the June 1982 and September 1983 cruises, the patterns are very similar to the March 1984 case. That is, the events of southward flow anomalies are short-lived and confined primarily above 100 m.

Other indirect evidence of intermittent southward flow along LBB is available. A Seasat synthetic aperture radar (SAR) image of this area taken on 27 September 1978 is reproduced in Fig. 6 (Fu and Holt, 1982). This image clearly shows a trail of small (∼20 km diameter) cyclonic vortices which originate at the southwestern corner of Grand Bahama Island (the shoreward ends of sections 6 and 7a in Fig. 1) and continue to the south across the western end of NWPC. The same SAR image also shows an apparent zone of strong surface current shear located 10–12 km from the edge of LBB. The location of this surface shear zone is in reasonable agreement with a similar shear zone measured by the ADCP in March 1984 (Fig. 3). A total of 11 SAR images are available over Grand Bahama Island from July to October 1978 (Holt, 1986, personal communication). In three of the passes, high

winds mask any details of the current structure. Of the remaining eight images, some indication of eddies off LBB can also be seen in those for 30 September and 3 October. It is unclear whether these eddies were newly formed or were simply the remains of those observed on 27 September.

The existence of southward flow near LBB and the possible presence of small-scale vortices within NWPC during this time may account for the complicated current structure seen in ADCP sections 7a and 7b across NWPC. In particular, the flow observed in March 1984 was the reverse (i.e., eastward in the northern half of NWPC and westward in the southern half) of that observed in earlier studies (Richardson and Finlen, 1967). Since southward flow events are highly intermittent, we cannot say anything from our data about the "typical" current structure in NWPC.

APPENDIX
Simple Modal Solutions to the Slanted-Boundary Problem

The simple model depicted in Fig. 7 can be used to examine the generation of modes in a stratified flow past a lateral boundary, the latter assumed to have a sudden change in orientation over part of its depth. A Cartesian x, y, z (up) coordinate system is used with y to the north. The following assumptions apply to the model:

1) A space- and time-independent northward geostrophic flow, $\bar{v}$, is present in a region bounded to the east by a vertical wall, but unbounded both to the west and in y;

2) This region has constant depth H, and the water within it is stably stratified with stability frequency $N(z)$;

3) The top and bottom boundaries are rigid;

4) At $x = 0$, a vertical wall is present over the whole depth for $y < 0$. For $y > 0$, the wall is inclined to the y axis by angle α for depths $-H < z < -\delta$ while continuing northward at shallower depths;
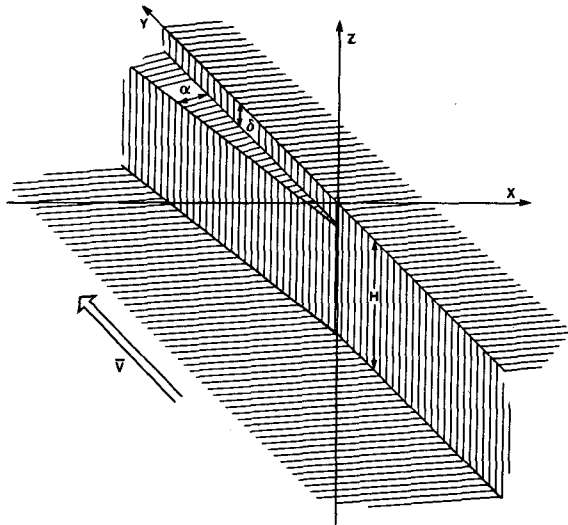
5) The flow is inviscid.

FIG. 7. Geometry of the model described in the Appendix.

Under the Boussinesq approximation, the linearized, steady-state equations for conservation of momentum (east, north, vertical), mass, and energy are

$$\bar{v}\frac{\partial u}{\partial y} - fv = -\frac{\partial P'}{\partial x} \qquad \text{(A1a)}$$

$$\bar{v}\frac{\partial v}{\partial y} + fu = -\frac{\partial P'}{\partial y} \qquad \text{(A1b)}$$

$$b = \frac{\partial P'}{\partial z} \qquad \text{(A1c)}$$

$$\frac{\partial u}{\partial x} + \frac{\partial v}{\partial y} + \frac{\partial w}{\partial z} = 0 \qquad \text{(A1d)}$$

$$\bar{v}\frac{\partial b}{\partial y} + N^2 w = 0, \qquad \text{(A1e)}$$

where f is the (constant) Coriolis parameter, $\rho_T = \rho_0 + \rho(x, y, z)$ is total density, ρ_0 is a constant reference density, and $P(=\rho_0 P')$, b $(=. -g\rho/\rho_0)$, u, v and w are respectively the perturbation pressure, buoyancy, and east, north and vertical velocity components. The boundary conditions to be applied to these equations are

$$w = 0 \quad \text{at} \quad z = 0, -H; \quad \text{all } x, y; \qquad \text{(A2a)}$$

$$u, v, w, P' \text{ and } b = 0 \quad \text{for} \quad y < 0; \qquad \text{(A2b)}$$

$$u, v, w, P' \text{ and } b \to 0 \quad \text{as} \quad x \to -\infty \quad \text{for} \quad y \geq 0; \qquad \text{(A2c)}$$

$$u(0, y, z) = u_0 h(y)h(-z - \delta) \quad \text{at}$$

$$x = 0, \quad \text{for} \quad -H < z < 0; \qquad \text{(A2d)}$$

where δ is the depth of the boundary step, h is the unit step function, and $u_0 = -\bar{v} \tan\alpha$. We assume $\alpha \ll 1$.

Equation (A1a–e) can be combined for a single equation in pressure:

$$\nabla_H{}^2 P' + \left(f^2 + \bar{v}^2\frac{\partial^2}{\partial y^2}\right)\left[\frac{\partial}{\partial z}\left(\frac{1}{N^2}\frac{\partial P'}{\partial z}\right)\right] = 0, \qquad \text{(A3)}$$

where $\nabla_H{}^2 = (\partial^2/\partial x^2) + (\partial^2/\partial y^2)$. Combining Eqs. (A1c) and (A1e), the vertical boundary condition [Eq. (A2a)] is

$$\frac{\partial P'}{\partial z} = 0 \quad \text{at} \quad z = 0, -H \qquad \text{(A4a)}$$

while the horizontal momentum equations give for the boundary condition on u at $x = 0$ $(y > 0)$:

$$f^2 u_0 h(-z - \delta) = -\left(f + \bar{v}\frac{\partial}{\partial x}\right)\frac{\partial P'}{\partial y}. \qquad \text{(A4b)}$$

Letting $P'(x, y, z) = {}_H P(x, y) \cdot {}_v P(z)$ in Eq. (A3), one obtains two separated equations for the vertical and horizontal structure of the pressure field:

$$\frac{d}{dz}\left(\frac{1}{N^2}\frac{d_v P}{dz}\right) + \lambda_v P = 0, \qquad \text{(A5a)}$$

$$\nabla_H{}^2({}_H P) - \lambda\left(f^2 + \bar{v}^2\frac{\partial^2}{\partial y^2}\right){}_H P = 0, \qquad \text{(A5b)}$$

where λ is a separation constant. Equations (A5a, b) must satisfy the following boundary conditions:

$$\frac{d}{dz}{}_v P = 0 \quad \text{at} \quad z = 0, -H, \qquad \text{(A6a)}$$

$$_H P \to 0 \quad \text{as} \quad x \to -\infty, \quad y > 0, \qquad \text{(A6b)}$$

$$_H P = 0 \quad \text{for} \quad y < 0, \qquad \text{(A6c)}$$

$$f^2 u_0 h(y)h(-z - \delta) = -{}_v P\left(f + \bar{v}\frac{\partial}{\partial x}\right)\frac{\partial_H P}{\partial y} \quad \text{at} \quad x = 0. \qquad \text{(A6d)}$$

Equation (A5a) has as solutions an orthonormal set of eigenfunctions, $\hat{\phi}_n(z)$, with eigenvalues λ_n, where $d\hat{\phi}_n/dz = 0$ at $z = 0$, $-H$. From Eq. (A6d),

$$_v P(z) = \sum_{n=1}^{\infty} \hat{A}_n \hat{\phi}_n(z) = h(-z - \delta) \qquad \text{(A6e)}$$

for the boundary condition. Using the orthonormality of the $\hat{\phi}_n$, the eigenmode amplitudes are given by

$$\hat{A}_n = \int_{-H}^{0} \hat{\phi}_n(z)h(-z - \delta)dz. \qquad \text{(A7)}$$

For each eigenmode, one can solve Eq. (A5b) for the corresponding horizontal structure ${}_H P_{(n)}(x, y)$. Laplace transforms of Eq. (A5b) and boundary condition [Eq. (A6d)] are, respectively:

$$\frac{d^2}{dx^2}{}_H P_{(n)} - T_n{}^2 {}_H P_{(n)} = 0, \qquad \text{(A8a)}$$

$$u_0 f^2 = -s^2\left(f + \bar{v}\frac{d}{dx}\right){}_H P_{(n)} \quad \text{at} \quad x = 0, \qquad \text{(A8b)}$$
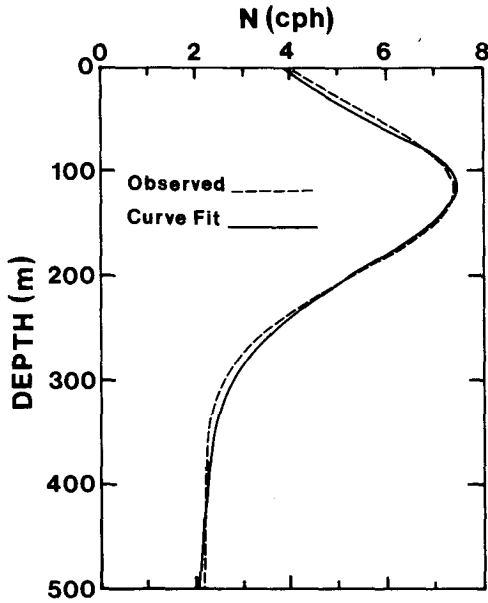
N (cph)

FIG. 8. Observed average vertical profile of stability frequency, N, in the eastern Straits of Florida. The dashed line shows the curve fit to N used in the model.

where

$$_H P_{(n)}(x; s) = \int_0^\infty {}_H P_{(n)}(x, y) e^{-sy} dy$$

and $T_n^2 = \lambda_n f^2 - s^2(1 - \lambda_n \bar{v}^2)$. The solution of Eq. (8a) which decays to zero as $x \to -\infty$ and satisfies Eq. (8b) is

$$_H P_{(n)} = - \frac{f^2 u_0}{s^2(f + \bar{v} T_n)} e^{T_n x}. \qquad (A9)$$

The inverse Laplace transform then gives the horizontal structure of the nth mode as

$$_H P_{(n)}(x, y) = -u_0 f^2 \left[\frac{1}{2\pi i} \oint \frac{e^{T_n x + sy}}{s^2(f + \bar{v} T_n)} ds \right]. \qquad (A10)$$

The contribution to this contour integral by the second-order pole at $s = 0$, which is of main interest here since it represents the response for large y (after the initial transients have propagated away), is given by

$$_H P_{(n)}(x, y) = -f u_0 y \frac{e^{f \sqrt{\lambda_n} x}}{(1 + \bar{v} \sqrt{\lambda_n})}. \qquad (A10a)$$

Using the result shown in Eq. (A10a) the solutions P', u, v, w and b are

$$P'(x, y, z) = -f u_0 y \sum_{n=1}^\infty \hat{A}_n \frac{e^{f \sqrt{\lambda_n} x}}{1 + \bar{v} \sqrt{\lambda_n}} \hat{\phi}_n(z); \qquad (A11a)$$

$$u(x, y, z) = u_0 \sum_{n=1}^\infty \hat{A}_n e^{f \sqrt{\lambda_n} x} \hat{\phi}_n(z); \qquad (A11b)$$

$$v(x, y, z) = -f u_0 y \sum_{n=1}^\infty \hat{A}_n \frac{\sqrt{\lambda_n} e^{f \sqrt{\lambda_n} x}}{1 + \bar{v} \sqrt{\lambda_n}} \hat{\phi}_n(z); \qquad (A11c)$$

$$w(x, y, z) = \frac{f u_0 \bar{v}}{N^2} \cdot \sum_{n=1}^\infty \hat{A}_n \frac{e^{f \sqrt{\lambda_n} x}}{(1 + \bar{v} \sqrt{\lambda_n})} \frac{d \hat{\phi}_n(z)}{dz}; \qquad (A11d)$$

$$b(x, y, z) = -f u_0 y \sum_{n=1}^\infty \hat{A}_n \frac{e^{f \sqrt{\lambda_n} x}}{(1 + \bar{v} \sqrt{\lambda_n})} \frac{d \hat{\phi}_n(z)}{dz}. \qquad (A11e)$$

As a specific example, eigenmodes have been computed using the following regression fit (to simplify the integration) to the observed N profile at PEGASUS stations in the eastern half of the Straits of Florida.

$$N = N_0 + N_1 e^{-\gamma^2 (z + z_0)^2}, \qquad (A12)$$

where $N_0 = 2.17$ cph, $N_1 = 5.23$ cph, $\gamma^2 = 7.73 \times 10^{-5}$ m^{-2} and $z_0 = 120$ m. Figure 8 shows this fitted profile together with the average N profile observed at PEGASUS station 8.

The first five eigenmodes, $\hat{\phi}_n(z)$, and their associated eigenvalues are shown in Fig. 9. The eigenmodes as shown have not been normalized but rather have been set to unit amplitude at the surface. The dimensionless eigenvalue, λ'_n, has been scaled by the water depth H
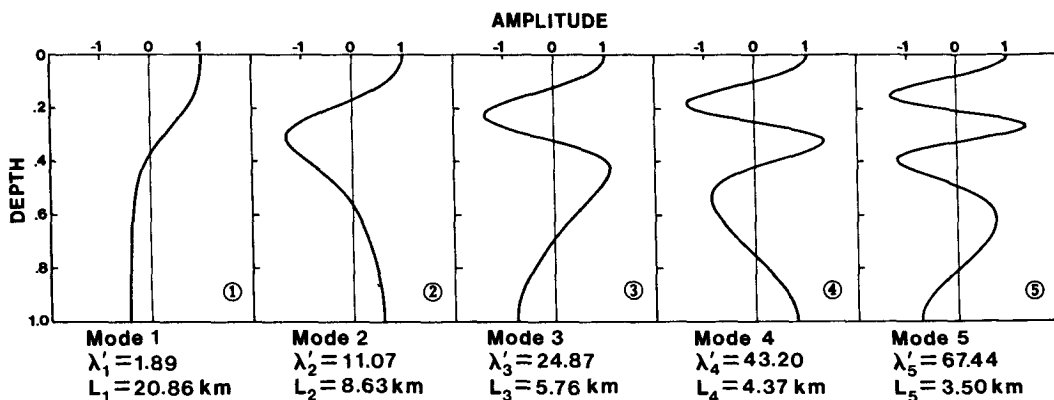
AMPLITUDE

Mode 1	Mode 2	Mode 3	Mode 4	Mode 5
$\lambda'_1 = 1.89$	$\lambda'_2 = 11.07$	$\lambda'_3 = 24.87$	$\lambda'_4 = 43.20$	$\lambda'_5 = 67.44$
$L_1 = 20.86$ km	$L_2 = 8.63$ km	$L_3 = 5.76$ km	$L_4 = 4.37$ km	$L_5 = 3.50$ km

FIG. 9. Lowest five vertical modes computed from the model using the N distribution shown in Fig. 8. The scaled eigenvalue, λ'_n, and e-folding decay scale, L_n, are also shown, the latter based on a 500 m depth.

and stability frequency constant N_0; therefore λ_n' = $H^2 N_0^2 \lambda_n$. The e-folding decay scale in x for each mode, $L_n = (N_0/f)(H/\sqrt{\lambda_n'})$, is also given in Fig. 9, with $f = 6.6 \times 10^{-5}$ s^{-1} and using a value of 500 m for the water depth. This depth corresponds roughly to the break in bottom slope at the foot of Little Bahama Bank.

Finally, Fig. 10 shows the baroclinic response of the east and north velocity components for the following choice of parameters: $\alpha = 20°$, $\delta = 30$ m, $\bar{v} = 0.5$ m s^{-1}, $x = -12$ km, and $y = 25$ km. Only the first five modes are included since for a position 12 km away from the boundary the contributions from higher modes are negligible.

A comparison of these curves with the observed average currents (Fig. 2) can only be qualitative for several reasons. First, α for the actual LBB is not small, thus introducing some uncertainty in the meaning of "distance offshore." Locally at 27°N, a 12 km distance from LBB would fall between PEGASUS stations 7 and 8. Second, the y distance (25 km) is somewhat arbitrary. If one assumes the inertial transient (in y) will substantially be propagated away from the boundary over a northward distance equivalent to that in which particles would be advected by the mean flow in one-half an inertial period (13.2 h at 27°N), then with $\bar{v} = 0.5$ m s^{-1} this distance is 23.8 km. Finally,

LBB is not of infinite north–south extent, as is the model boundary.

Within these limitations, however, some features of the model can also be seen in the observations. In particular, the shear in both model and observations is concentrated in the depth region of maximum N. Relative to the flow below this region, the baroclinic model v component decreases and the u component increases as the surface is approached, also in agreement with the observations. Finally, the 21 km east–west decay scale of the largest amplitude (lowest) mode is in reasonable agreement with, for example, the lateral decay scale observed in the u component (Fig. 2).

The baroclinic model flow is essentially independent of depth below 200 m, whereas the observed velocity components decrease toward the bottom. A probable explanation for this is that the actual mean northward flow (treated as a constant, $\bar{v}$, in the model) has some baroclinicity near the boundary (as it clearly does farther west in the core of the Florida Current) and itself decreases with depth.

REFERENCES

Fu, L.-L., and B. Holt, 1982: Seasat views oceans and sea ice with synthetic-aperture radar. Jet Propulsion Lab Pub. 81–120, 200 pp.

Hine, A. C., R. J. Wilber, J. M. Bane, A. C. Neumann and K. R. Lorenson, 1981: Off-bank transport of carbonate sands along open, leeward bank margins: Northern Bahamas. Mar. Geol., 42, 327–348.

Larsen, J. C., and T. B. Sanford, 1985: Florida Current volume transports from voltage measurements. Science, 277, 302–304.

Leaman, K. D., and P. S. Vertes, 1983: The Subtropical Atlantic Climate Study (STACS), 1982, summary of RSMAS "PEGASUS" observations in the Florida Straits. Tech. Rep. UM RSMAS No. 83012, 154 pp.

——, R. L. Molinari and P. S. Vertes, 1987: Structure and variability of the Florida Current at 27°N: April 1982–July 1984. J. Phys. Oceanogr., 17, 565–583.

Lee, T. N., 1977: Coastal currents along the southern shore of Grand Bahama Island. Bull. Mar. Sci., 27(4), 803–820.

——, F. Schott and R. Zantopp, 1985: Florida Current: Low-frequency variability as observed with moored current meters during April 1982 to June 1983. Science, 227, 298–302.

Marmolejo, E., 1985: Baroclinic tides in the Straits of Florida. M.S. thesis, University of Miami, Rosenstiel School of Marine and Atmospheric Science.

Maul, G., F. Chew, M. Bushnell and D. Mayer, 1985: Sea level variation as an indicator of Florida Current volume transport: Comparisons with direct measurements. Science, 277, 304–307.

Mayer, D. A., K. D. Leaman and T. N. Lee, 1984: Tidal motions in the Florida Current. J. Phys. Oceanogr., 14(10), 1551–1559.

Molinari, R. L., 1983: STACS: Subtropical Atlantic Climate Studies. Eos, Trans. Amer. Geophys. Union, 64(2).

——, W. D. Wilson and K. Leaman, 1985: Volume and heat transports of the Florida Current: April 1982 through August 1983. Science, 227, 295–297.

Niiler, P. P., and W. S. Richardson, 1973: Seasonal variability of the Florida Current. J. Mar. Res., 31(3), 144–166.

Richardson, W. S., and J. R. Finlen, 1967: The transport of Northwest Providence Channel. Deep-Sea Res., 14, 361–367.

Schott, F., and R. Zantopp, 1985: Florida Current: Seasonal and interannual variability. Science, 227, 308–311.

Spain, P. F., D. L. Dorson and H. T. Rossby, 1981: PEGASUS: A simple acoustically tracked velocity profiler. Deep-Sea Res., 28A, 1553–1567.
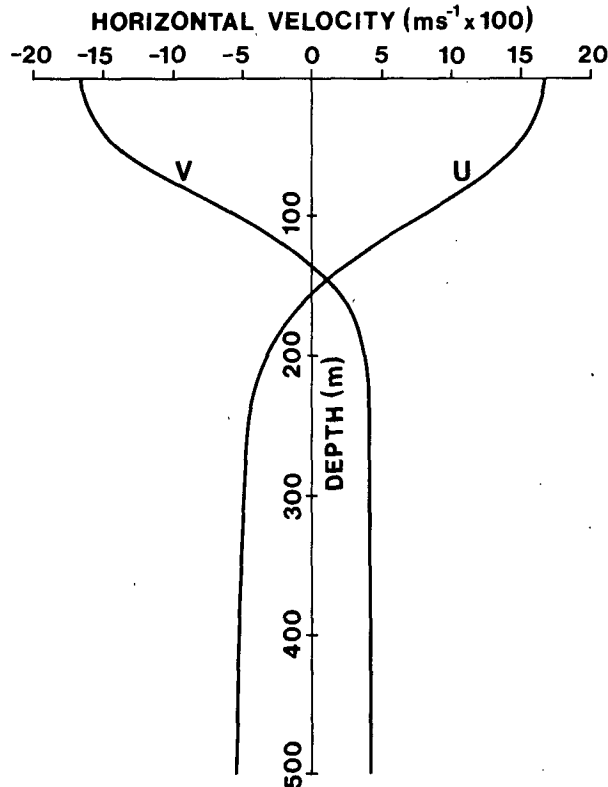
HORIZONTAL VELOCITY (ms^{-1} x 100)

FIG. 10. East (u) and north (v) velocity components generated from the five modes shown in Fig. 9. Parameters used to generate these profiles are given in the Appendix.